Automatika

Journal for Control, Measurement, Electronics, Computing and Communications

ISSN: (Print) (Online) Journal homepage: https://www.tandfonline.com/loi/taut20

Induction motor's rotor slot variation measurement using logistic regression

J. Anish Kumar, N. M. Jothi Swaroopan & N. R. Shanker

To cite this article: J. Anish Kumar, N. M. Jothi Swaroopan & N. R. Shanker (2022) Induction motor's rotor slot variation measurement using logistic regression, Automatika, 63:2, 288-302, DOI: 10.1080/00051144.2022.2031541

To link to this article: https://doi.org/10.1080/00051144.2022.2031541

Published online: 04 Feb 2022.

AUTOMATIKA
2022, VOL. 63, NO. 2, 288–302
https://doi.org/10.1080/00051144.2022.2031541

Induction motor's rotor slot variation measurement using logistic regression

J. Anish Kumar [a], N. M. Jothi Swaroopan[b] and N. R. Shanker[c]

[a]Electrical and Electronics Engineering, Saveetha Engineering College, Chennai, India; [b]Electrical and Electronics Engineering, RMK Engineering College, Gummidipoondi, India; [c]Department of Computer Science and Engineering, Aalim Muhammed Salegh College of Engineering, Chennai, India

ABSTRACT

Rotor slots in induction motor expand due to thermal imbalance and create magnetic stress. Magnetic stress is a force that develops on the laminated surface of the rotor due to the curving or stretching magnetic flux. Traditional motor fault detection methods never measure magnetic stress on the rotor; a significant problem frequently arises in the motor. Magnetic stress is proportional to slot size variations in the rotor. High slot size variations on the laminated surface of the rotor lead to more curving and stretching magnetic flux and damage the rotor and stator, reducing their efficiency and induce harmonics. In this paper, the Average rotor Slot Size Variation (ASSV) in the rotor is predicted during the running condition of the motor through logistic regression. Logistic regression predicts ASSV by multimodal sensor signal sub-band energy values and measures rotor slot sizes from microscope images. Multimodal sensor signal is obtained from various sensors, such as vibration, temperature, current and Giant Magneto Resistance (GMR). Signal sub-band energy is obtained from Over complete Rational-Dilation Wavelet Transform (ORaDWT). From experimental results, ASSV is more than 75% from standard size, damaging the rotor and stator. The accuracy of ASSV prediction is about 92%.

ARTICLE HISTORY
Received 10 September 2021
Accepted 14 January 2022

KEYWORDS
Induction motor; rotor slot; rotor slot variations; GMR sensor; logistic regression

1. Introduction

Motor works based on magnetic interlinking between stator and rotor. The stator comprises a cylindrical frame in the outer region, magnetic path, and electrical winding with insulation. It consists of lamination and slots; lamination is fabricated with high-grade alloy steels. Lamination in the stator reduces eddy current and heating. The stator coils are excited when the motor is powered. In a 3-phase induction motor, three sets of coils are inside the stator lamination with 120° of separation. The rotor always keeps rotating coaxially with the stator, when the motor is connected to the power supply. Figure 1 shows magnetic field line flow in squirrel cage motor and magnetic stress [1].

In the squirrel cage induction motor, the rotor is in a squirrel cage structure. The squirrel cage rotor interacts with magnetic fields in the stator and leads to torque formation. In the squirrel cage motor, bars in the rotor are designed based on speed–torque requirement. In the three-phase induction motor, the rotor is the most important component and experiences high thermal [2] and magnetic stress due to inrush current, overload, Transient, High voltage and current, low voltage due to single phasing and current. This stress leads to rotor stress [3].

During high-speed running condition motor, the centrifugal force and thermal stress are increased on the rotor surface. Permanent magnet motor has high compressive strength (800Mpa), and is brittle [4]. The stress in the rotor is calculated by numerical and analytical methods. The analytic method of rotor stress measurements [5–7] has a major drawback, i.e. assuming the rotor is in rotational symmetry. In [6,8] the displacement method was adapted for rotor stress calculation. Some analytical methods include axial stress [9] for rotor stress calculation and never consider edging effect and geometry discontinuity. Rotor stress calculation is more complicated due to non-linear factors and complicated structure. Moreover stress is not measured by temperature [10] during over speed and low speed concerning magnet tangential and radial stress. However, rotor sleeve thickness and rotor outer diameter are calculated with traditional designs [3]. The magnetic force on the rotor slot increases due to the double power frequency current [11]. This force leads to leakage magnetic flux in rotor slots [11–15] and moves towards the bottom of slots.

Significant stresses in the rotor are thermal, magnetic, and mechanical. These stresses need to be monitored and should be at a tolerant level for the long run

CONTACT J. Anish Kumar janishengg@gmail.com Electrical and Electronics Engineering, Saveetha Engineering College, Saveetha University, Chennai 600077, Tamil Nadu, India

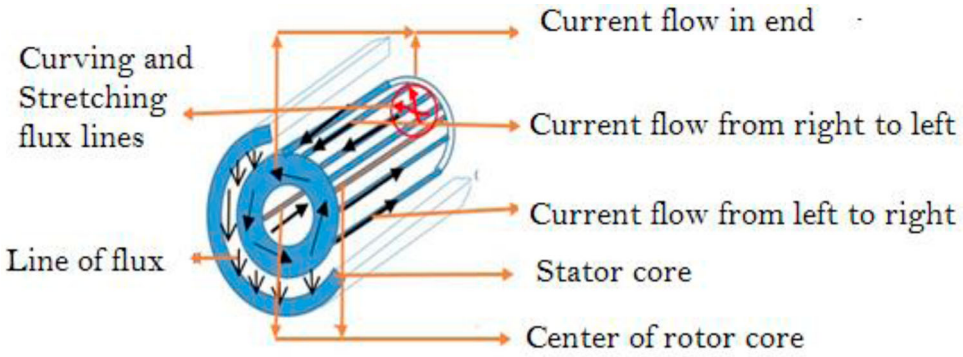

Figure 1. Magnetic stress and current flow in the squirrel cage rotor.

of motor, without failures. The failures in an induction motor are stator, rotor, and bearing fault. The bearing and stator fault reduces through regular maintenance. Rotor faults can be prevented from regular monitoring of thermal and magnetic stresses in the motor during running conditions [16]. Rotor faults reduce by admitting a tolerant level of thermal and magnetic stresses on the motor [17]. These stresses cause a significant fault in the rotor system and simultaneously damage the stator. The thermal stress in the rotor of the squirrel cage induction motor arises due to frequent starting of the motor, vibration from the improper fixation of shaft and rotor, high starting current, negative sequencing current, uneven current circulation, rotor bowing and hot spots in the rotor. Moreover, rotor sparking arises because of thermal stress and damages the stator [18]. Furthermore, magnetic stress leads to rotor failures such as rotor bar bend, fatigue failure, heavy noise, and more vibration. Magnetic stress forms because of leakage flux from rotor slots' size variation and generates dynamic force proportional to the square of rotor current, which vibrates the rotor bar [19]. High vibration in the rotor leads to misalignment between shaft and bearing. Rotor vibration makes the rotor in an unbalanced position and may even hit the stator and causes damage.

Thermal and magnetic stresses are the major reasons for rotor and stator faults [18]. Thermal stress can be identified through visual interpretation of rotor and stator [19–21]. Rotor and stator under abnormal thermal stress exhibit melted regions on rotor-laminated surfaces. The rotor shows thermal stress through hot spots in its outer surface, melted paint, melted air passage, and bowing in rotor laminations [21,22]. Moreover, magnetic stress inside a motor is detected at the initial stage. Magnetic stress in the rotor is monitored for healthy running conditions and reduced harmonics. However, magnetic stress-based failure identification is very difficult in squirrel cage induction motors. Physical evidence for magnetic stress is the rub spot on the rotor. Magnetic stress leads to rubbing spots because of contact between the rotor and stator [23,24]. When magnetic stress does not create any physical contact between the rotor and stator, the identification of magnetic stress becomes very challenge. Magnetic stress is due to high current, overload, transient, high voltage and current, low voltage and current and thermal imbalance between the rotor and lamination leading to sparking. The high sparking period in the motor reduces its lifetime by damaging the rotor bar and end rings. Magnetic stress is due to curving, and stretching magnetic flux lines from rotor slots' size variation vibrates rotor bar and misaligns rotor position radially. Magnetic stress is due to leakage flux from rotor slot, pulls rotor from the centre and creates more vibration [25]. Magnetic stress rotates the rotor in different axes, leads to shaft bend, and damages the stator. Table 1 shows different sensor locations in the motor for rotor fault detection. However, existing rotor fault detection methods never addressed magnetic stress. The induction motor performance is investigated due to the end ring faults [26]. Deep learning-based motor fault detection can provide reliable solutions for industries [27]. The sliding mode observer technique detects rotor current faults. This method proves fast response and better stability than the existing method [28]. By the three-phase current intersection signals, the induction motor rotor fault is diagnosed for high- and low-load motor operations [29]. A convolution neural network with batch normalization detects the bearing and broken rotor bars fault in squirrel cage induction motors [30].

A. Inference from literature survey

Researchers identify rotor faults, such as rotor bar misalignment, unbalanced rotor, and rotor induction measured through various sensors such as current, voltage, flux sensor and visual inspection. However, the rotor experiences high thermal stress and magnetic stress on its laminated surface. Thermal stress is measured through temperature measurement. However, magnetic stress over rotor lamination needs to be measured. The magnetic stress forms due to the magnetic flux line curving and stretching between rotor and stator. The curving and stretching magnetic flux lines result from

Table 1. Different sensor locations in motor for rotor fault detections.

Sensors/ref	Problems	Location of sensors
Current sensor/[9]	Rotor faults during the low frequency of torque oscillations	Input supply
Flux sensor/[30]	Rotor bar fault mixed with eccentricity	Hall effect sensors inserted inside the rotor
Current and voltage sensor/[7]	Unbalanced rotor fault	Input supply
Voltage and current probes /[10]	Wound rotor induction fault	Input voltage and currents
Vibration sensor /[12]	Rotor bar fault	shaft vibration signal
Current, Temperature Vibration sensor GMR sensor **[Proposed]**	***Identification of optimum sensor location for acquiring curving and stretching (CS) flux from rotor slots and measuring magnetic stress through Average rotor slot size variation (ASSV)***	***Motor End shield, Drain, Input current***

rotor slot size variation at the surface of rotor lamination. Rotor slot variation measurement needs to be done during the running condition of the motor. Magnetic stress over rotor lamination is the major root cause for all rotor faults.

B. Problem statement

Now and then, rotor faults, such as bar fault, unbalanced rotor fault, rotor surface damage, are detected in induction motor by various sensors, such as current, vibration, GMR and voltage. Sensor signals are analysed based on threshold levels of voltage, signal spectrum, or current signature analysis for rotor fault detection. Moreover, researchers concentrate more on stator and bearing faults detection. However, the rotor is the major source for all faults in the motor, such as bearing, shaft, and stator. Moreover, thermal and magnetic stresses in the rotor are the root cause for all types of rotor faults. Magnetic stress from rotor slot variations must be monitored to avoid destructive sparking, leakage flux and rotor damages. Measuring magnetic stress in the rotor is still a challenging task. For monitoring and measuring magnetic stress, rotor slot size variation during the running condition of the motor need to be measured. The major problem in magnetic stress measurement would be the identification of the appropriate location of the sensor for acquiring curving and stretching magnetic flux lines.

C. Contributions

Destructive sparking and vibration in the motor result from magnetic stresses, such as curving and stretching magnetic flux lines. High Magnetic stress in the rotor leads to the variable radial position of the rotor during running conditions of the motor, and hits the stator [18]. Radially rotating rotor generates more leakage flux from the laminated surface of rotor and rotor slots [20] and develops excessive centrifugal forces. To avoid magnetic stress in the rotor, ASSV is predicted during running conditions of the motor.

(i) Curving and Stretching magnetic flux lines from the rotor slot are analysed through manually created rotor slots such as 3 and 9 mm on the lamination surface, and the optimum location of GMR sensor on the motor is identified by the oscillatory behaviour of the above flux. From the GMR sensor signal the relation between CS magnetic flux lines and slot size variations in the rotor is identified. Moreover, acquired sensor signals with white and unscaled noises are filtered by the proposed Non-Decimated Discrete Stationary Wavelet Transform (NDSWT).

(ii) Sensor signals are obtained from the motor during various induced faults, such as inrush current, frequent starting, different load conditions, high current and radially positioned rotor in motor for analysing the behaviour of stretching and curving flux through the sub-band energy values obtained from Over complete Rational-Dilation Wavelet Transform (ORaDWT).

(iii) To predict ASSV, a Logistic regression model is used. Logistic regression uses Energy band values of sensor signals and measured rotor slot values from microscope images for ASSV prediction during running conditions of the motor.

In this paper, magnetic stress is measured through Average rotor Slot Size Variation (ASSV), since magnetic stress is proportional to rotor slot size variation. For ASSV measurement, various sensors are used, such as temperature, current, vibration and GMR sensors. LM335 temperature sensor measures rotor temperature, the motor current signature is analysed through a toroidal sensor (Model no. SCT013). The vibration of the rotor is measured through the ADXL335 sensor, which measures free, forced, and dampen vibrations in the rotor due to magnetic stress. AA002-02 GMR sensor measures magnetic field strength over 3 CM distance with a minimum sensitivity of 0.45 mV/V-Oe. Curving and stretching (CS) flux from the rotor due to variation in rotor slot size is measured by the GMR sensor. The GMR sensor is fixed in the front side of the motor, and it collects CS flux magnetic lines. The GMR sensor is fixed very close to the rotor side of drain in the motor. The vibration sensor is kept at the end bearing gap and acquires rotor unbalancing vibration due to magnetic stress. Similarly, to measure high-

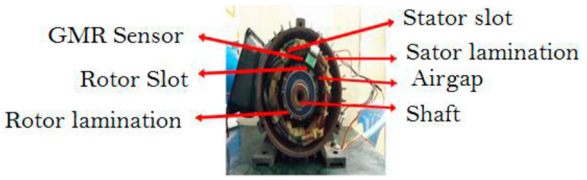

Figure 2. GMR sensor fixed in between rotor and stator air gap for measuring CS flux.

and low-input current, the current sensor is fixed to the input power supply. Thermal stress is measured through a temperature sensor located at the drain, close to the rotor. The GMR sensor is fixed in between the rotor and stator air gap, as in Figure 2.

II. Materials and methods

The induction motor consists of air ducts for various applications, such as cooling, rotor weight reduction and reduced metal. Axial duct creates magnetic reluctance asymmetrically as the path for flux, whereas the shaft provides an alternate path for magnetic flux. Flux path varies according to the magnetic field and air ducts; such variations lead to magnetic reluctance in the motor and influence magnetizing current. Magnetizing flux affects the frequency of flux, leads to vibration, and varies the current spectrum. Magnetic flux overlaps with stray and leakage flux, which arise due to rotor damage or air gap eccentricity. Furthermore, frequent starting of the motor and high current during underload conditions leads to high heat and magnetic stress on rotor bars. Subsequently rotor slot sizes varys and generate CS flux due to thermal and magnetic stress. Heat over the rotor bars expands the rotor slot. High current in the rotor expands bars and makes a variation in the resistance value of lamination of rotor and rotor slots size. An uneven thermal and magnetic stress on the rotor bar leads to a change in magnetic reluctance in the rotor slots and leads to sparking. Such sparking in motor for a period damages rotor bar such as crack, broken bar and rub the spot. However, the sparking period decides the nature of sparking, such as defective or non-defective. Furthermore, the major reason for the fault in the rotor is due to magnetic and thermal stresses. Thermal stress causes heat in the rotor during running conditions and leads to uneven expansion of rotor slots. An uneven expansion of rotor slots creates CS flux in the rotor. CS flux due to the uneven expansion of rotor slot leads to the low air gap and form magnetic flux density with harmonic content. To study slot size variations in the rotor due to thermal imbalance needs multimodal sensors signals. Acquired signals' statistical parameter helps detect motor faults, such as destructive sparking various radially positioned rotor-running conditions and analyse the oscillatory behaviour of CS flux. Flux signal due to rotor slot size variation is studied through the appropriate location of GMR sensor in motor. The location for the GMR sensor is the air gap region near the rotor, identified after studying the oscillatory behaviour of CS flux from induced rotor slots such as 3 and 9 mm. CS flux travel inside the rotor due to the property of flux linkages and such flux can be collected from the material contact region of the motor, i.e. shaft region of the motor. CS flux travels between slots in the rotor, parallel to the entire rotor surface. CS flux moves out in the air gap due to uneven expansion of the rotor slot. Therefore, the optimum solution for placing the GMR sensor is fixed near the shaft region because the CS flux travels to both ends of the rotor. From GMR sensor signal analysis, the maximum of CS flux is obtained from the front end of the motor, i.e. on the drain. For ASSV prediction, sensor signals collected from different locations, such as vibration sensor, are kept in a non-drive end shield, GMR, temperature sensors at the drain region of the motor, and high current in motor measures through the current sensor. Figure 3 shows a methodology diagram for predicting ASSV, through which CS flux is monitored and measured.

Sensor signals are acquired through a 3-Dimensional Digital acquisition board. Figure 3 shows rotor slots images from microscope Smars® HD 1920 × 1080P USB Digital Microscope camera. A microscope camera is used for measuring slot variations before and after induced faults in the motor. The various induced faults in the motor are different load conditions, variable input currents, and voltages, different radial positions of the rotor and manually created slots such as 3 and 9 mm.

A. Data acquisition system (DAQ) for multimodal sensor signal acquisition

USB data acquisition system consists of a Digital Class-B amplifier. USB data acquisition has four analogue channels and a data controller. The data controller collects signals from sensors, buffers data in the controller, and transfers them to the personal computer. The buffer in the Data acquisition system holds 984-bit samples and 512–984-bit length in size, based on the number of samples per packet. The analogue channels acquire signals up to 1200 samples per second with 300 scans per second for high-speed acquisition. The analogue channels are of 12-bit resolution. The supply voltage of DAQ is +3.6V. DAQ acquired signals sent to MATLAB software for analysis.

B. Experimental procedure for magnetic stress analysis in rotor slots

Thermal and magnetic stress are analysed through signals acquired from various sensors. Sensor signals are

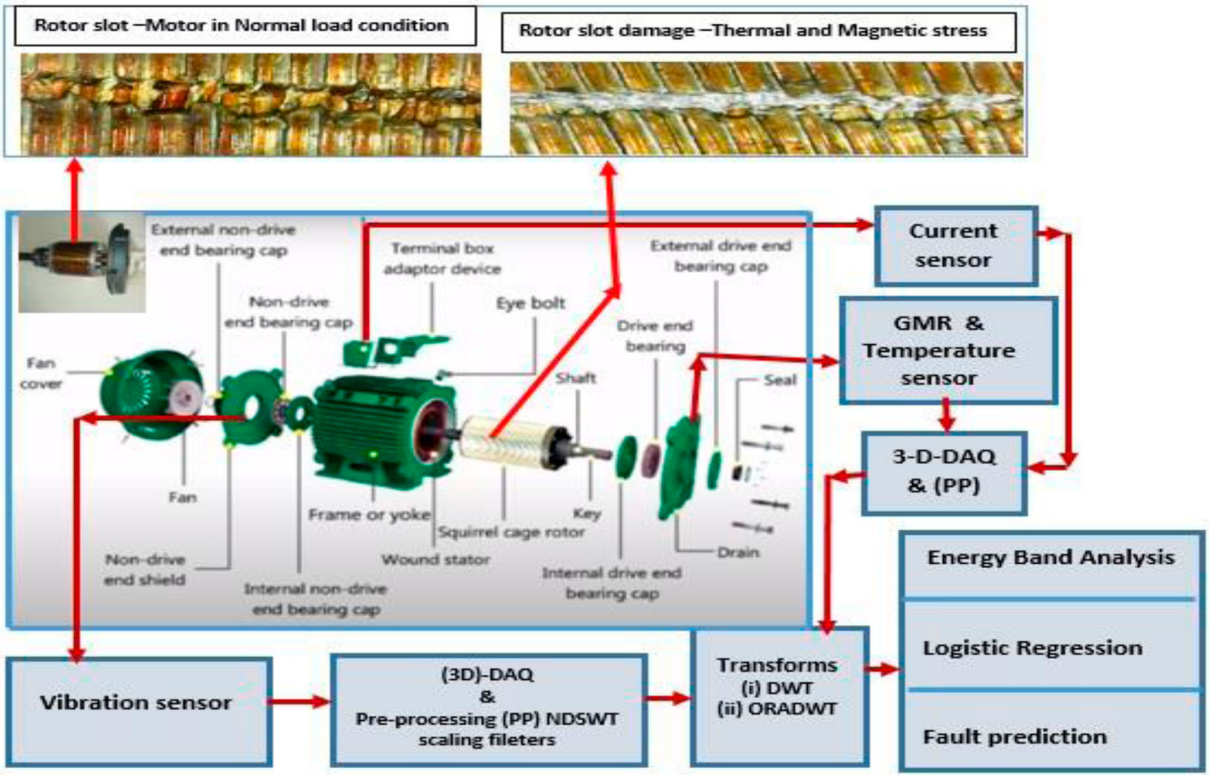

Figure 3. Methodology for predicting average rotor slot size variation (ASSV) in induction motor for monitoring and measuring CS flux.

acquired from the motor at different input parameters such as current ranging from 1.5 to 5 A, voltage ranging from 180 to 450 V, motor speed ranging from 1400 to 1500 rpm, and load is varied from 0 to 17 kg. During running conditions of the motor, CS flux is created through induced faults such as transient fault, over and under load, variable input current and voltage. Sensor signals, such as temperature, GMR, current and vibrations, are acquired through a USB-3D-DAQ card and MATLAB Data acquisition toolbox. After each and every induced fault, signals from sensors are acquired and the rotor is removed immediately, for acquiring images of rotor slots through a Smars® HD 1920 × 1080P USB Digital Microscope camera. The rotor slot image is used for measuring slots variation after every induced fault in the motor through pixel measurements. The pixel-based length measurements of rotor slots helps identify average slot variations after every induced fault. For example, induced transient fault is created by frequent disconnection of voltage through fast ON and OFF switching for continuous 5–10 min and the rotor gets the maximum of high current during every switching. After every switching period, CS flux-based stress is seen through the increase in amplitude, temperature and current signal, and the rotor is removed from the motor within 180–240 s for acquiring microscopic images. In a similar method, 2500 signals from each sensor are acquired, and their respective rotor slot images are acquired for measuring Average rotor Slot Size Variations. These signals acquired through a 3-Dimensional data acquisition system are pre-processed with a Non-Decimated Discrete Stationary Wavelet Transform filter.

C. NDSWT scaling filter for white and unscaled noises

The DAQ acquired sensor signals are white and unscaled noise. White noise arises due to uncorrelation in successive samples during the acquisition of magnetic, vibration and current signals. In acquired signals all frequency components are in a similar bandwidth. The white noise in signals is in the form of random signals with similar intensity, variable frequencies, and with constant power spectral density. The white noises in the vibration signals are sequential with time and flat spectrum. The unscaled noises are spatially correlated with arbitrary correlation. The unscaled noises are added in signals according to sensor location in the motor. For example, the GMR sensor located in the rotor region acquires stator leakage flux. To avoid unscaled noises, the optimum location of sensors in the motor plays a vital role. In the proposed ASSV prediction, white and unscaled noises are filtered through the NDSWT. The NDSWT fills the gap created during the decimation process of the discrete wavelet transform through shift-invariant property and redundant frequency information is obtained from signals. The NDSWT identifies te stationary and non-stationary signals collected from sensors. The NDSWT

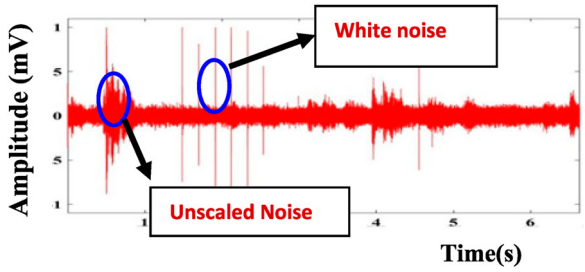

Figure 4. GMR sensor signal during overload condition of the motor.

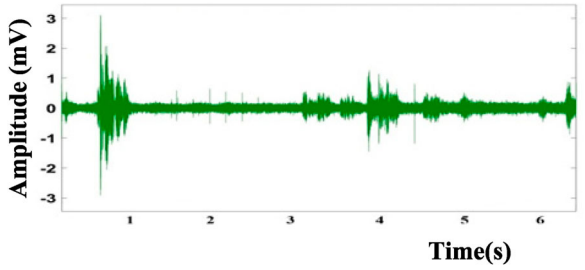

Figure 5. NDSWT filtered GMR sensor signal during the overload condition of the motor.

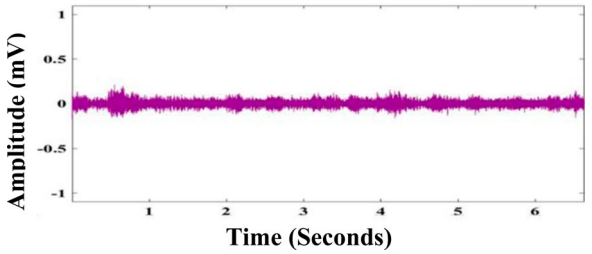

Figure 6. DWT filtered GMR sensor signal during overload.

is based on the sensitivity of choice in the starting point for a time series, i.e. Shift-invariant. The sensitivity is due to downsampling of the signal at each stage. Figure 4 shows GMR sensors signal with white noise and unscaled noise during overload conditions. The acquired signals from the motor are pre-processed for reducing white and unscaled noises, which arise during signal acquisition. The sensor signals are pre-processed through traditional algorithms such as Discrete Wavelet Transform (DWT). Figure 5 shows GMR sensor signals filtered with DWT. Figure 6 shows NDSWT filtered GMR signal. Table 2 shows the performance of various filtering algorithms such as DWT and FFT to reduce white and unscaled noises. From statistical analysis, the NDSWT filter performs better for GMR, vibration and current sensor signals, whereas the DWT performs better for temperature signals due to less white noise.

White and unscaled noises are very high in GMR and Vibration sensor signals. Higher white noise variation in GMR and Current sensor signals need NDSWT filtering. The NDSWT is more suitable for filtering all sensor signals. NDSWT filtered signal is given as input to the ORaDWT algorithm for energy band analysis.

D. Over complete rational-dilation wavelet transforms (ORaDWT)

The acquired signals from motor, such as current, vibration and flux signals, are piecewise smooth that need effective transform for analysis. The various transforms such as DWT, RaDWT, Dyadic perform less due to low-frequency resolution, i.e. low Q-factor. The oscillatory behaviour of CS flux signal from the GMR sensor is analysed through Over complete Rational-Dilation Wavelet Transforms (ORaDWT). ORaDWT applies over completeness through increased sampling rate in frequency and time with a high range of redundancy factors. ORaDWT performs based on non-dyadic dilations flexible range of Q-factors and obtains redundancy factors. The proposed ASSV prediction uses ORaDWT for all acquired sensor signals. In the ORaDWT algorithm, frequency bands are represented in numbers, after passing through bandpass filters and interlaced to form subband signals. Furthermore, the frequency domain approach is through polynomial matrix factorization. ORaDWT performs better than dyadic transform due to high Q-factor and improves resolution for shot time-periodic k oscillatory signals.

Let us consider

$$U(\omega) = X(a\omega) \tag{1}$$

$$V(\omega) = \frac{1}{b}F(\omega)U(\omega) + F\left(\omega + \frac{2\pi}{b}\right)U\left(\omega + \frac{2\pi}{b}\right) + F\left(\omega + (b-1)\frac{2\pi}{b}\right) \times U\left(\omega + (b-1)\frac{2\pi}{b}\right) \times F^*(\omega) \tag{2}$$

$$Y(\omega) = \frac{1}{a}V\left(\frac{\omega}{a}\right) + V\left(\frac{\omega}{a} + \frac{2\pi}{a}\right) + V\left(\frac{\omega}{a} + (a-1)\frac{2\pi}{a}\right) \tag{3}$$

$$U\left(\frac{\omega}{a} + k\frac{2\pi}{b} + n\frac{2\pi}{a}\right) = X\left(\omega + ak\frac{2\pi}{b}\right) \tag{4}$$

$$Y(\omega) = \sum_{k=0}^{b=1} Ck(\omega)X\left(\omega + ak\frac{2\pi}{b}\right) \tag{5}$$

$$Ck(\omega) = \frac{1}{ab}\left[F\left(\frac{\omega}{a} + k\frac{2\pi}{b}\right)F^*\left(\frac{\omega}{a}\right) + F\left(\frac{\omega}{a} + k\frac{2\pi}{b} + \frac{2\pi}{a}\right)F^*\left(\frac{\omega}{a} + \frac{2\pi}{a}\right) + F\left(\frac{\omega}{a} + k\frac{2\pi}{b} + (a-1)\frac{2\pi}{a}\right) \times F^*\left(\frac{\omega}{a} + (a-1)\frac{2\pi}{a}\right)\right] \tag{6}$$

Table 2. Performance of different filters for various sensor signals.

Sensor signal	Faults	Algorithm	Means	Standard deviation	Median
GMR	Overload	DWT	1.2452	3.8291	4.239
Vibration	Transient	NDSWT	1.3744	3.3886	4.470
Temperature	High Current	FFT	1.1672	3.5789	3.9645
Current	High Voltage	NDSWT	1..4475	3.3987	4.6235
GMR	Low Voltage	DWT	1.3247	3.1549	4.1235
Vibration	Low Current	FFT	1.2354	2.9789	3.1246
Temperature	Induced slot size increased	NDSWT	1.3987	3.4567	4.7892

The output of the filter bank is given by Equation (7):

$$Y(\omega) = \sum_{k=0}^{q-1} Lk(\omega) X\left(\omega + pk\frac{2\pi}{q}\right) + \sum_{k=0}^{s-1} Mk(\omega) X\left(\omega + k\frac{2\pi}{s}\right) \quad (7)$$

$$Lk(\omega) = \frac{1}{pq}\sum_{n=0}^{p=1} H\left(\frac{\omega}{p} + k\frac{2\pi}{q} + n\frac{2\pi}{p}\right) \times H^*\left(\frac{\omega}{p} + n\frac{2\pi}{p}\right). \quad (8)$$

$$M_{k(\omega)} = \&\frac{1}{s} G\left(\omega + k\frac{2\pi}{s}\right) G^*(\omega) \quad (9)$$

H(ω) represents low-pass filter, and G(ω) represents high-pass filter. Figure 7 shows Rational-Dilation wavelet transforms sampling, and Figure 8 shows the ORaDWT sampling method. The p/q is the dilation factor, which is a rational number.

$$\frac{p}{q} + \frac{1}{s} > 1 r\omega\epsilon\left[0, \left(1 - \frac{1}{s}\right)\frac{\pi}{p}\right] G(\omega)| = \sqrt{s} for \omega\epsilon\left[\frac{p}{q}\pi, \pi\right] \quad (10)$$

The NDSWT pre-processed vibration signal is given as an input signal to ORaDWT and RaDWT. Figures 9 and 11 show the percentage of energy sub-bands. Figures 10 and 12 show the reconstruction of the signal from ORaDWT and RaDWT. From simulated results, ORaDWT performs better than RaDWT due to more sub-band energy levels. Energy band values of ORaDWT are used for measuring rotor slot size variation.

III. Results and discussion

Rotor slot size variations due to high current, high voltage and frequent starting of the motor are experimented. The CS flux is generated due to Rotor slot size variations. Flux due to rotor slot size variation is detected through a multimodal sensor located at end shield and drain of the motor. To predict rotor slot size variation, energy band amplitude values from ORaDWT and rotor size variation measured from microscope camera values are correlated through logistic regression for prediction. An experimental result proves that all motor-induced faults vary the rotor slot sizes. The rotor slot size variations lead to harmonics and damage the stator. Further section discusses rotor size variations due to high current, variable conditions, non-radial position of the rotor and induced rotor slot variations more elaborately.

A. Rotor slot variations during high current and variable load conditions

The rotor slot variations during high current and variable load conditions are analysed through current, temperature, GMR, vibration sensors signals and microscope camera images of the rotor. To find rotor slot variations the motor is fed with the current of 1.5–5 A and signals are acquired from all sensors. For different load conditions, spring balance is varied from 0 to 17 kg. During different load conditions the temperature, GMR, vibration and current sensor signal amplitude are high and have random amplitude variations due to fluctuating CS flux. The Current sensor amplitude maintains a peak voltage (5 V) for high current and high load. Figure 13 shows various energy band levels obtained through the ORaDWT algorithm for GMR sensor signals. The sensor signals are acquired during different loads, speeds, and currents. From experimentation, sub-band energy levels show total variations in seven sub-bands. For each type of fault in the motor such as over current, overload, over speed, low current, low speed, improper fixing, non-radial conditions, induced harmonics, loose coupling between the motor and load, and transient faults shows variations between zero to seven in sub-bands. For certain faults, band variations are seen in two bands. The signals are collected from various sensors such as temperature, GMR, vibration, and current during load variation between 0 and –17 kg, line current between 1.5 and 5 A, load voltage between 180 and 490 V, motor speed between 1400 and 1500 rpm. Furthermore, Energy band values from ORaDWT and measured slot size variation from microscope camera image are obtained. Moreover, sensor signals are acquired during induced harmonics and transient faults. Harmonics are induced in the motor through series-connected inductor load creates sag and swell in the input voltage. Transient generators are used in this experiment to generate transient voltage. Transient generators were connected adjacent to the motor, which generates transient pulses in the supply voltage.

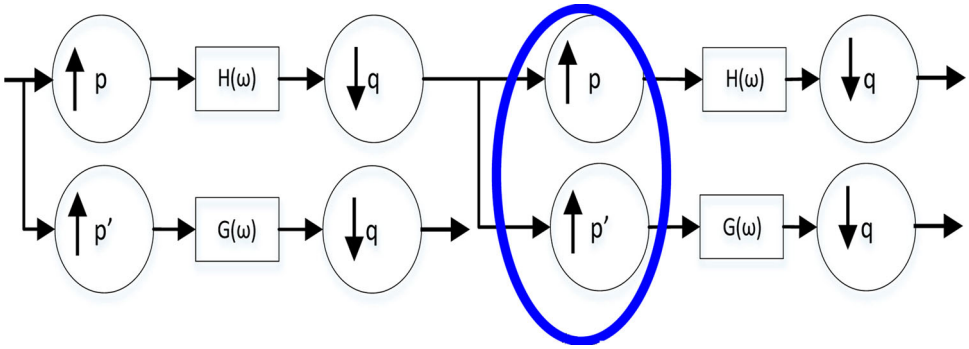

Figure 7. RaDWT – sampling the time-frequency.

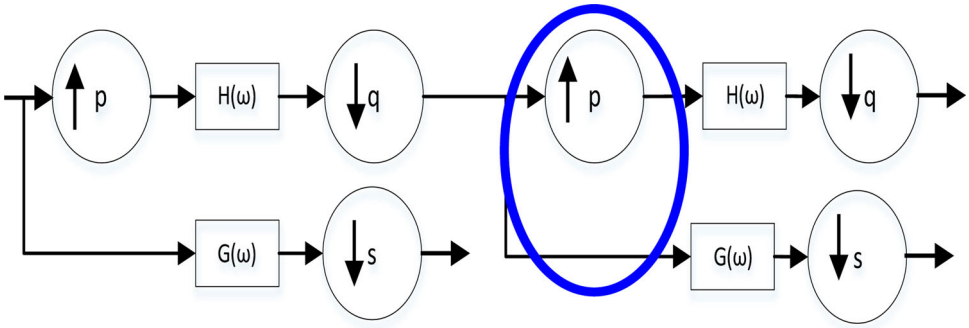

Figure 8. ORaDWT – sampling the time-frequency.

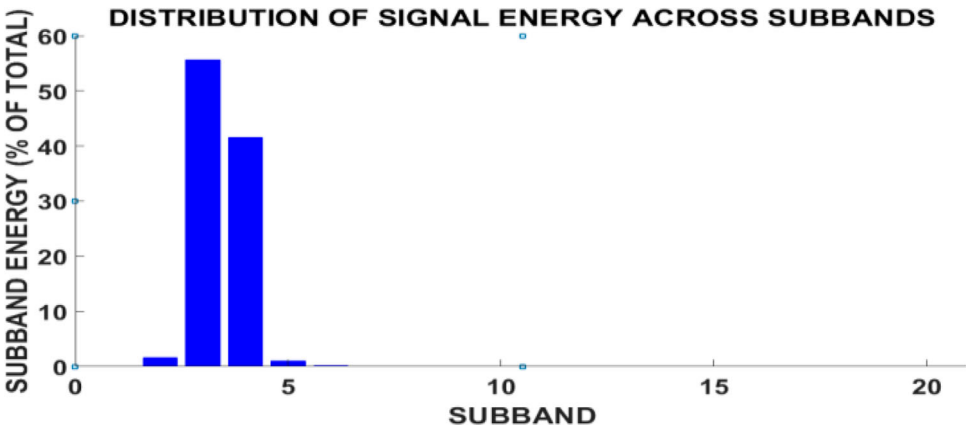

Figure 9. ORaDWT – vibration of the sensor signal (over load-condition).

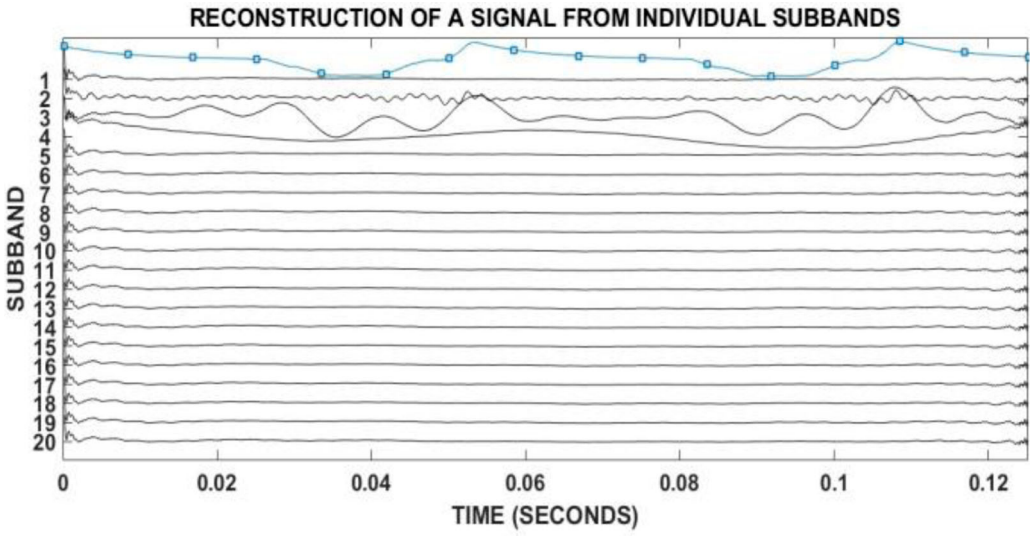

Figure 10. ORaDWT – sampling the time-frequency of vibration sensor signal at load-condition.

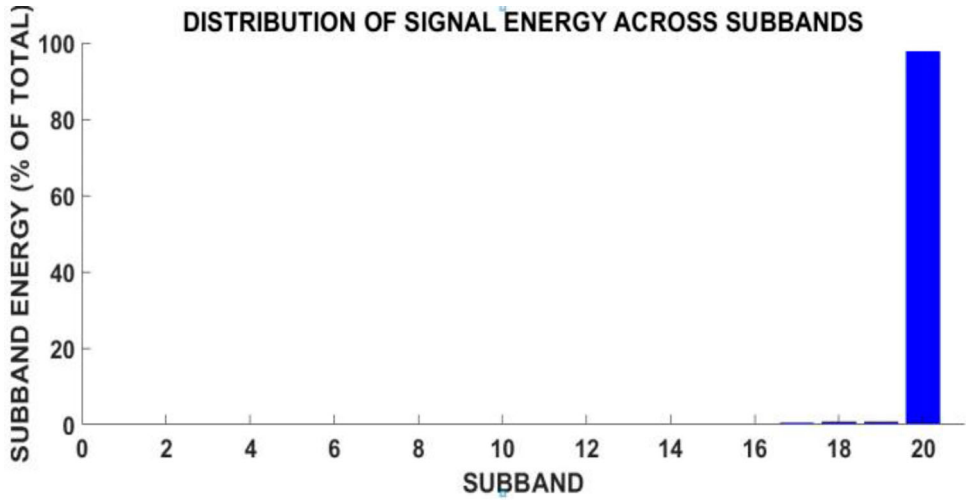

Figure 11. RaDWT of vibration sensor signal (over load-condition).

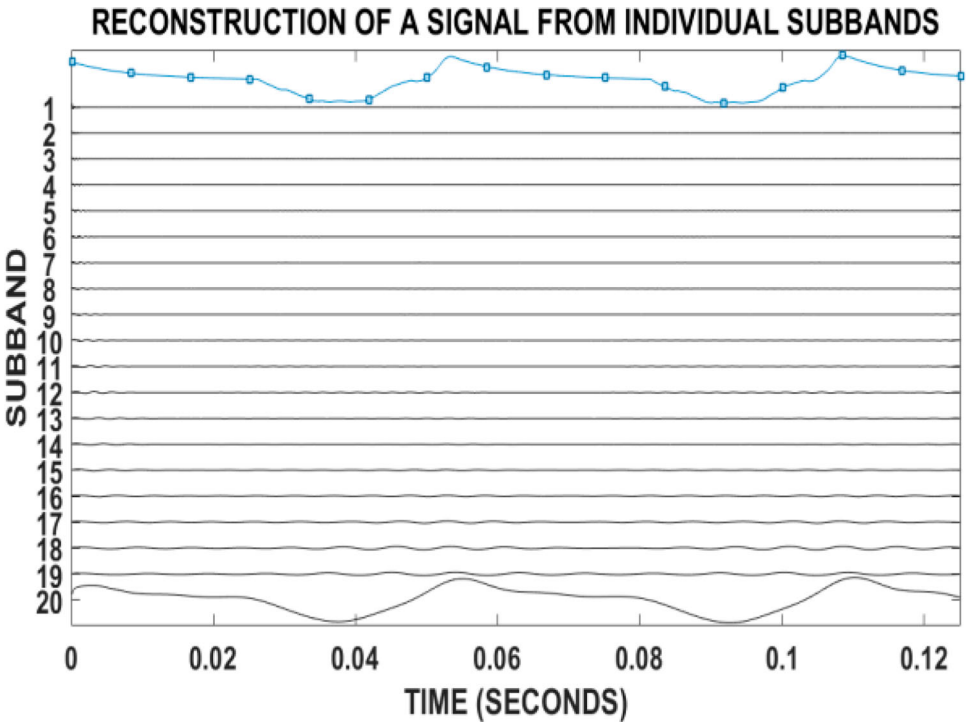

Figure 12. RaDWT – sampling the time-frequency of the motor vibration sensor signal at load-condition.

These pulses interfere in motors that are used for the experimental analysis. Figure 14 shows energy band variation of GMR sensor signals during low speed.

Figure 15 shows a microscopic image of the rotor slot taken from the Smars® HD 1920 × 1080P USB digital microscope camera. After every induced fault, the rotor in motor is removed and microscopic images obtained to measure the average slot variation in the rotor. The rotor image is obtained within 240 s and sometimes below the 240 s, so the maximum temperature in the rotor is maintained. Average rotor Slot Size Variations are measured through pixel measurements between gaps in slots in Figure 15. Furthermore,

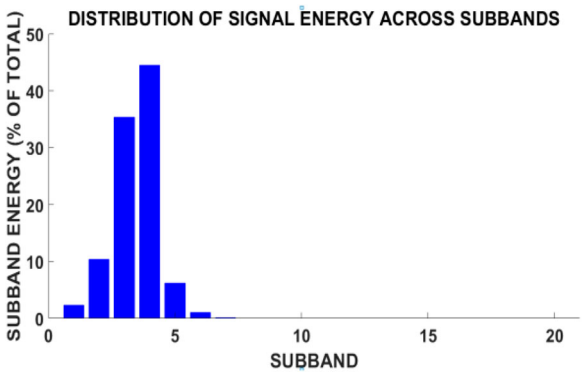

Figure 13. GMR signal at 415 V no-load condition.

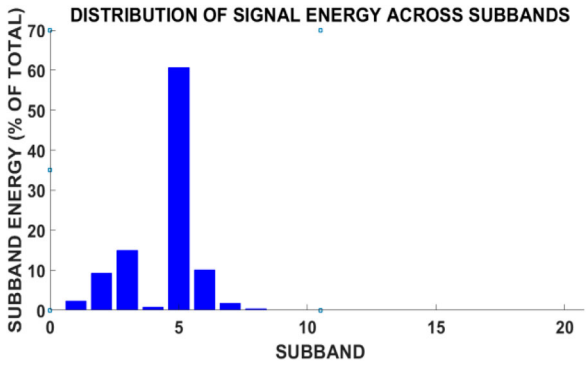

Figure 14. GMR signal at Low Speed over Load condition.

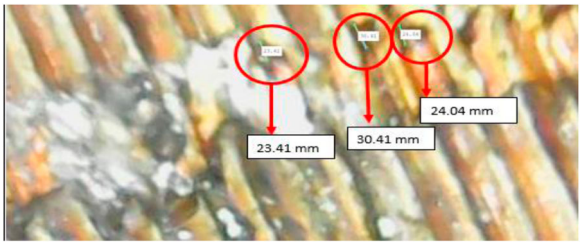

Figure 15. Microscopic image of the rotor slot with slot measurement.

rotor slot size variation is analysed through the non-radial position of the rotor in the motor during running conditions.

B. Rotor slot variations due to non-radial positions of the rotor

The non-radial position of the rotor in the motor is induced through bending shaft and loose fit of bearing. The shaft bending is done between 3° and 5°, whereas the acceptable bending of the shaft is about 0.04°. The bending for a higher degree in the shaft has more thermal stress in the rotor due to improper fixation of shaft and rotor. Due to the improper fixation of the rotor and frequent starting of the motor leads to high currents and uneven current circulations in rotor slots. The uneven CS flux is due to current circulation and detection through GMR sensor signals. Simultaneously, the vibration sensor signal shows variation in amplitude. During high starting current, vibration amplitude is high of about 3.5 V. The shaft bend leads to an amplitude voltage of 2.5 V from the vibration sensor. Furthermore, the signal pattern of the GMR sensor shows random variations due to the bend shaft. GMR signal is acquired from different locations of the motor such as stator side, and stator winding side, the random signals in GMR sensor signal are less when the GMR sensor is placed between the gap of the rotor and stator slots, show high random signal variations due to high CS flux. Figure 15 shows a microscopic image of the rotor slot captured 5 hr of continuous running of the motor with a shaft bend.

The frequent starting of the motor increases the vibration in the motor. Furthermore, improper fixation of shaft and rotor, high starting currents and high current increases slot size in the rotor. The CS increases due to rotor slot size variation and generates a dynamic force proportional to the square of rotor current, which vibrates the rotor. The high vibration in the rotor due to flux from varying rotor slot sizes leads to misalignment between shaft and bearing. The rotor vibration makes rotor in unbalanced position and causes damage in the rotor. Furthermore, motor under frequent start and high current under load condition leads to heat, damages the rotor slots and is seen through microscope images as in Figures 16 and 17. Subsequently, rotor slots size variations generate CS flux due to thermal stress on the motor. In the next section, CS flux over slots is analysed by induced rotor slots.

C. Induced rotor slot variations for magnetic stress analysis

To study the effect of variations in rotor slots, the rotor in the motor is induced with two slots in irregular directions, as shown in Figures 18 and 19. CS flux is analysed through an induced rotor slot of 3 mm and measured through a microscope image. Figure 19 shows an induced rotor slot of 9 mm. Initially, a 3 mm induced rotor slot is kept in the motor and tested in different conditions such as overload, overcurrent, load, and no load. Sensor signals are analysed for energy bands. GMR and temperature signals show a big difference in amplitude and slight changes in vibration. The energy band for the GMR sensor signal is shown in Figures 18 and 19 for 3- and 9 mm-induced slots, respectively.

Furthermore, the rotor with 9 mm-induced slots tested under different load conditions and their corresponding signals and sub-band energy levels are analysed for CS flux behaviour. GMR energy band signals for 9 mm slot show more bands (8) as shown in Figure 19. Moreover, the percentage of sub-band energy of the signal is high for 3 mm-induced slot as in Figure 18. The energy band variations show more CS flux as slot size increases. CS flux signals increase bands numbers for the higher size of induced slots. Table 3 shows different induced faults and corresponding values of rotor slot size variation energy band. The identification of stress due to CS flux needs a multimodal sensor. In Table 3, the energy band signal amplitude values are shown for respective induced faults. Table 3 shows the faults and their respective sensors value required for measuring CS flux stress in the motor, and these sensor values need to be acquired at the same time and duration. However, thermal stress in the rotor region is identified through a temperature sensor, CS flux stress over rotor surface needs GMR, current and vibration signals. During rotor slot size

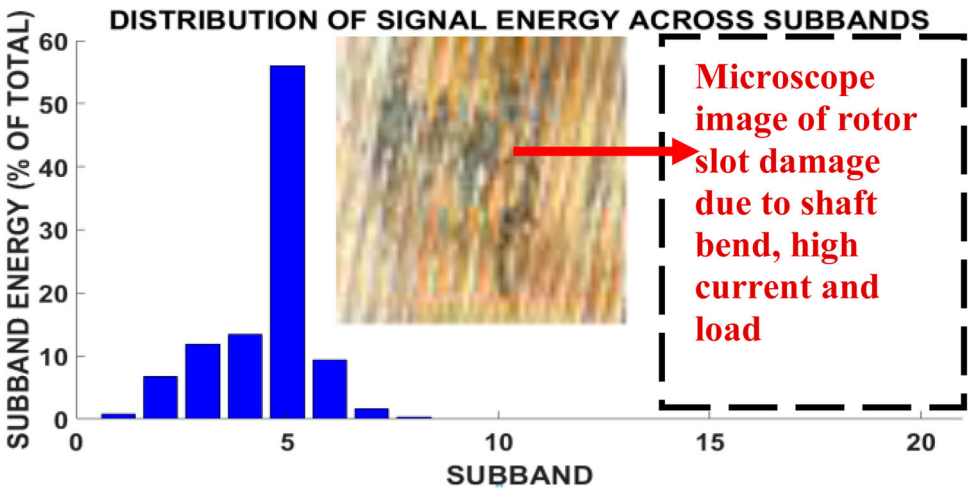

Figure 16. Sub-band energy diagram of GMR signals for shaft bend.

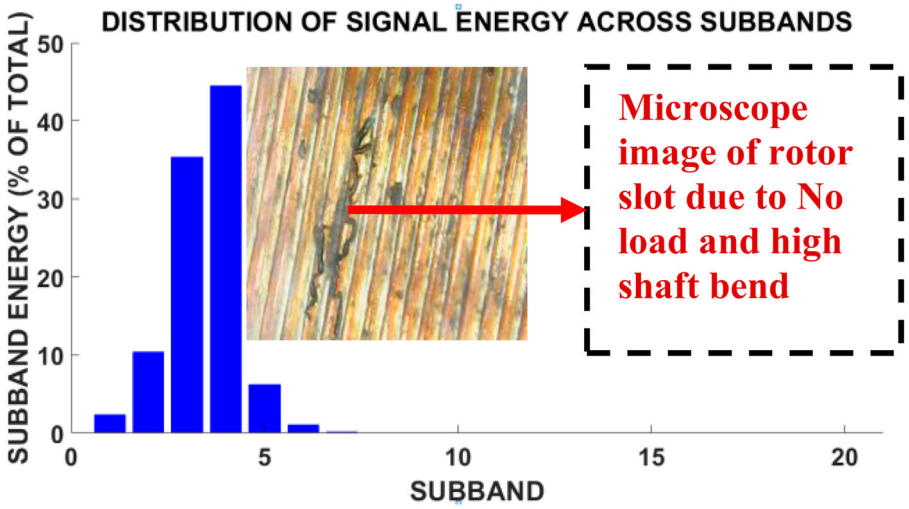

Figure 17. Subband energy diagram of GMR signals for high current and no-load condition.

variation, temperature and GMR sensor signals' amplitude are high, and randomness in signal is seen very clearly, and slowly vibration and current sensor signals show variations in the signal. High variations in rotor slot size are due to CS flux stress and thermal stress. All sensor values show a sudden rise in their energy band amplitude values when CS flux stress increases and is confirmed through induced 9mm rotor slot size. Whereas for induced harmonics, the current sensor signal shows high variation, and other sensors never show any change. For transient faults, vibrations and current sensor signals show a higher change in energy band

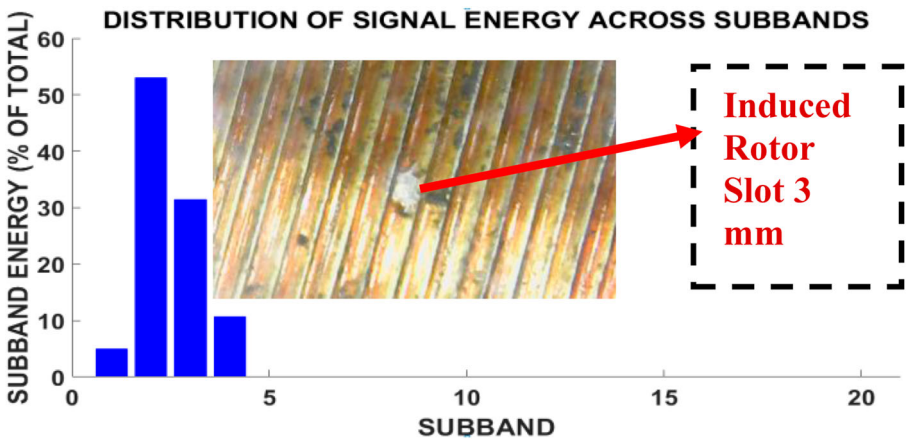

Figure 18. Energy band of GMR signal for induced slot (3mm).

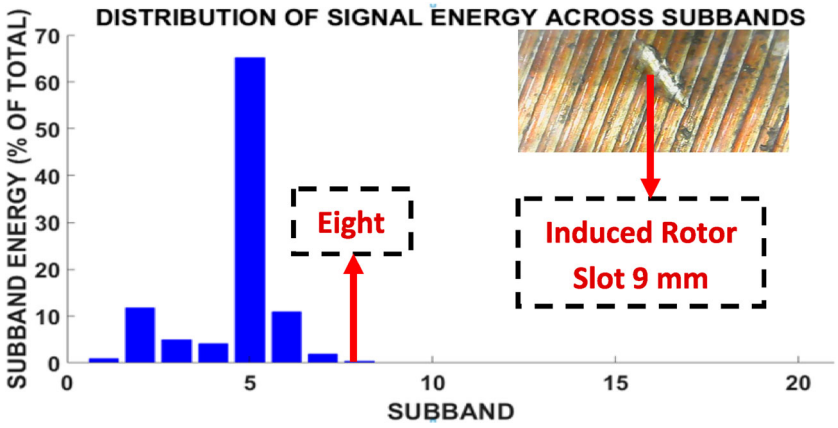

Figure 19. Energy band of GMR signal for induced slot (9mm).

Table 3. Probabilistic values for the proposed prediction method.

Predictor	Coefficient	Estimate	Standard error	t-statistic	*p*-value
Constant	$\beta 0$	25.1835	1.2145	20.7365	0.0002
V (SEAV)	$\beta 1$	3.8761	1.4961	2.5907	0.081
T (SEAV)	$\beta 2$	0.3332	1.3696	0.2433	0.8235
I (SEAV)	$\beta 3$	15.4796	2.7863	5.5557	0.0115
G (SEAV)	$\beta 4$	−14.8516	2.6657	−5.5713	0.0114

amplitude values, whereas other sensor signals never show much variation. For bearing faults, vibration sensors signal show a high difference in their energy band amplitude values. Moreover, stator fault is identified through vibration sensors and current sensors signals. However, CS flux stress in the motor is identified through multimodal sensor energy band values-based Average rotor Slot Size Variation predictions. For measuring, Average rotor Slot Size Variations in rotor need all sensor values and prediction algorithm.

D. Predication of Average rotor slot size variation through logistic regression

Multinomial logistic regression method is the extension of the Logistic regression method and is used for more than two classes of the dependent variable. The logistic regression method is a complement of linear regression for categorizig the target variable. For a dependent variable Y with two class and predictor variable X let g(x) = Pr(X = x) = 1-Pr(X = x), Logistic regression consists of a linear form for Logit with probability as in Equation (11):

$$\text{Logit}[g(x)] = log\left(\frac{g(x)}{1-gx)}\right) = \alpha + \beta x \qquad (11)$$

where the odds $= \frac{g(x)}{1-gx}$

Logit is a linear approximation and equal to the logarithm of the odds. β represent rate of increase or decrease in the S-shaped curve of g(x). Logistic regression extended to models with multiple predictor variables. Let μ represent the number of predictors for a binary variable Y as $x1, x2 \ldots x\mu$. The model for log-log odds is as in Equation (12):

$$\text{Logit}[PrPr(T = 1)] = \alpha + \beta 1x1 + \beta 2x2 + .+\beta\mu x\mu \qquad (12)$$

and h(x) is given as Equation (13):

$$h(x) = \frac{\exp(\alpha + \beta 1x1 + \beta 2x2 + \cdots + \beta\mu x\mu)}{1 - \exp(\alpha + \beta 1x1 + \beta 2x2 + \cdots + \beta\mu x\mu)} \qquad (13)$$

The βi,for 1 < i ≤n and 1 < j . n and $i \neq j$ which represents the effect of xi on log-odds

T = 1, controls the other xj, for example, exp (βi)is the multiplicative effect on odds of a one-unit which increases the xi, at a fixed level of other xj. If "n" independent observations with "n" predictor variables and target variable consist of q categories, to build the Logits in the multinomial, one of the categories considered as a base level and Logits functions constructed relative to base level. Let H_j represents the multinomial probability of *j*th category, the relationship between this probability and the n-predictor variables, $X1, X2 \ldots X\mu$, the multinomial logistic regression model is as in Equation (14):

$$\log[\frac{Kj(xi)}{Kz(xi)} = \alpha_{01} + \beta_{1j}x_{i1} + \beta_{2j}x_{i2} + \cdots + \beta_{\mu j}x_{\mu i} \qquad (14)$$

where j = 1,2,… .z-1 and i = 1,2,… n. Since all the H's adds to unity, this reduces to

$$loglog(H_j(x_i)) = \frac{exp(\alpha_{01} + \beta_{1j}x_{i1} + \beta_{2j}x_{i2} + \cdots + \beta_{\mu j}x_{\mu i})}{1 + \sum_{j\leq 1}^{Z-1} \alpha_{01} + \beta_{1j}x_{i1} + \beta_{2j}x_{i2} + \cdots + \beta_{\mu j}x_{\mu i}} \qquad (15)$$

For j = 1,2,… z−1. The model parameters are determined by the multinomial linear method.

Prediction of laminated slot variation size in the rotor is done through logistic regression: a supervised learning method. The prediction of the target value is obtained from probability. The logistic regression

Table 4. Different motor faults and average rotor slot size variation in the rotor.

Induced faults	V (SEAV)	T (SEAV)	I (SEAV)	G (SEAV)	Band variation-sORaDWT	Average variation in rotor slot (mm)
Overload	0.4	0.6	0.5	0.6	3	26.23
Frequent starting	0.8	0.9	0.9	0.9	5	29.36
Transient fault	0.5	0.8	0.4	0.5	3	26.15
Non radial rotor	0.9	0.6	0.6	0.5	4	30.21
Shaft bend	0.6	0.6	0.6	0.4	2	31.25
Induced harmonics	0.8	0.4	0.4	0.4	3	29.14
Low speed	0.4	0.5	0.5	0.6	2	25.14
High speed	0.4	0.6	0.5	0.6	1	29.64
Induced slot on the rotor laminations	0.6	0.7	0.8	0.9	1 to 8	36.78

is classified as binary logistic regression and multinomial regression model. In binomial logistic regression, a variable is of two types: zero and one. Through such variables, the predication of success or failure is obtained. Multinomial logistic regression has more than three dependent variables. The prediction of Average rotor Slot Size Variations is done through multinomial logistic regression due to non-multi-collinearity in data, i.e. independent variables are independent of each other. Furthermore, energy band data are larger with no quantitative significance, sensor signal energy value data are in unordered types. From experimental analysis sensor signal energy values and measured values of rotor slot size obtained from microscopic images are used for ASSV prediction during running conditions of the motor. From Equation (16), slot average variations are predicted through Sub band Energy Amplitude Values (SEAV) of GMR, Vibration, Current, and Temperature. As given in Table 4 the experimental data prove that thermal stress creates magnetic variation. Furthermore, high current burns rotor lamination after attaining an extreme rotor slot size expansions. The extreme size of rotor slots size variation is seen through more energy bands, i.e more than seven energy bands from GMR sensor signals. Average rotor Slot Size Variation (ASSV) is as shown in Equation (16) (Figure 20).

$$\begin{aligned} \mathrm{ASSV} = {} & 25.1835 + 3.8761 * \mathrm{V(SEAV)} \\ & + 0.3332 * \mathrm{T(SEAV)} + 15.4796 * \mathrm{I(SEAV)} \\ & - 14.8516 * \mathrm{G(SEAV)} \end{aligned} \tag{16}$$

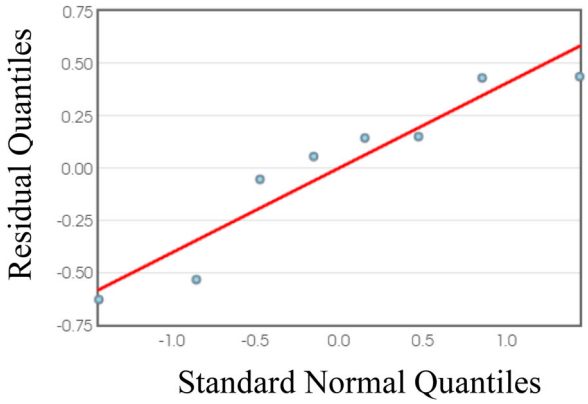

Figure 20. Residual plot for multinomial logistic regression of rotor slot variation.

The predicted ASSV values of the new motor are depicted in Table 5. Table 5 shows ASSV five three-phase induction motors under different running conditions, such as ideal, no-load, and loading conditions. For example, sample motor SM1 has 1.75 mm of rotor slot and during no-load condition, motor runs for 5 hr and rotor slot expands to 2.04 mm due to CS flux stress, whereas during load condition rotor slot expands to 3.25 mm after the continuous running of motor for 5 hr. The ASSV Equation (16) predicts rotor slot variation. If the rotor slot expands more than 75% of the original size, i.e. 3.25 mm slot expands to 5.68 mm size, the motor has more CS flux stress.

IV. Conclusion

The rotors are prone to high thermal and magnetic stress during running conditions due to inrush

Table 5. Performance evaluation of the proposed ASSV prediction in different motors.

Sample motor (SMx)	Ideal condition – average rotor slot size in (mm) (microscope image)	No-load conditions – average rotor slot size in (mm) (microscope image)	Load condition – average rotor slot size in (mm) (microscope image)	Expanding of rotor slot (%)	ASSV – prediction under-load condition (mm) (ASSV – logistic regression)/prediction accuracy (%)	CS flux level in the motor
SM1	10.75	20.04	30.15	80%	3.03/96%	High
SM2	20.14	20.87	40.06	90%	3.80/93%	High
SM3	30.50	30.78	50.95	70%	5.45/91%	Medium
SM4	10.50	10.87	20.25	50%	2.03/90%	Low
SM5	20.48	20.94	30.47	40%	3.29/94%	Low

current, overload, over-current, frequent starting, transient fault, non-radial rotor, shaft bend, harmonics, and high speed. The magnetic stresses need to be monitored and should be in the tolerant level for the long run of the motor, without failures. In this paper, magnetic stress on rotor slot is analysed through various sensor signals, such as temperature, GMR, current and vibration. The appropriate locations of the sensor in motor, such as Non-drive end shield, drain, and terminal box, are identified through induced rotor slots such 9 and 3 mm energy band signal analysis. From acquired sensor signals, energy band values are obtained through band spectrum and identified through ORaDWT. Moreover, microscope images of rotor slots are used for measuring rotor slot sizes and verified with predicted ASSV for accuracy. The average slot expansion in the rotor leads to understanding magnetic stress over rotor slots. The ASSV is predicted during running conditions of the motor through logistic regression from sensor signal energy band values. The average expansion of rotor slot size exceeds more than 75% and needs maintenance. Maintenance improves the efficiency of the motor, maximum torque is maintained.

In the industrial environment, dismantling of stator and rotor during burnt or electrical smell is very frequent for mentioned motor duty cycles, such Continuous duty, Continuous duty with intermittent periodic loading, Continuous duty with starting and braking, and Continuous duty with periodic speed changes. The ASSV method measures slot variations, which are the major signs for all faults that arise in the motor during running states and prevent the faults at an earlier stage. In modern industries early motor faults detection increases production and minimizes the downtime. The proposed ASSV method avoids frequent dismantling for continuous duty cycle motor because of slot variation predictions. The proposed method performs less for the Short time duty, intermittent periodic duty, intermittent periodic duty with starting, intermittent periodic duty with starting and braking induction motors.

The proposed work can be extended with Nano coating over laminated sheets and can be monitored for CS flux through ASSV prediction values to evaluate the efficiency of the induction motor.

Acknowledgements

The authors would like to thank Mrs. S. Tamilselvi, Chase technologies for her support in image acquisition and experimental setup.

Disclosure statement

No potential conflict of interest was reported by the author(s).

ORCID

J. Anish Kumar http://orcid.org/0000-0002-1795-5538

References

[1] Gerlach ME, Zajonc M, Ponick B. Mechanical stress and deformation in the rotors of a high-speed PMSM and IM. Elektrotech Inftech. 2021;138:96–109. doi:10.1007/s00502-021-00866-5.

[2] Sikanen E, Nerg J, Heikkinen JE, et al. Fatigue life calculation procedure for the rotor of an embedded magnet traction motor taking into account thermo mechanical loads. Mech Syst Signal Process. October 2018;111:36–46. doi:10.1016/j.ymssp.2018.03.055.

[3] Wang Y, Zhu Z-Q, Feng J, et al. Rotor stress analysis of high-speed permanent magnet machines with segmented magnets retained by carbon-fibre sleeve. IEEE Trans Energy Convers. June 2021;36(2):971–983. doi:10.1109/TEC.2020.3022475.

[4] Huang Z, Fang J. Multiphysics design and optimization of high-speed permanent-magnet electrical machines for air blower applications. IEEE Trans Ind Electron. 2016;63(5):2766–2774. doi:10.1109/TIE.2016.2518121.

[5] Klohr M, Binder A, Schneider T. Fixation of buried and surface-mounted magnets in high-speed permanent-magnet synchronous machines. IEEE Trans Ind Appl. 2006;42(4):1031–1037.

[6] Xing J, Wang T, Wang F, et al. Optimization design of rotor structure for high-speed permanent-magnet machines. Proc Int Conf Elect Mach Syst. 2007: 1438–1442.

[7] Wu S, Huang X, He L, et al. Mechanical strength analysis of pulsed alternator air-core rotor. IEEE Trans Plasma Sci. 2019;47(5):2387–2392. doi:10.1109/TPS.2019.2891300.

[8] Borisavljevic A, Polinder H, Ferreira JA. On the speed limits of permanent-magnet machines. IEEE Trans Ind Electron. 2010;57(1):220–227. doi:10.1109/TIE.2009.2030762.

[9] Burnand G, Araujo DM, Perriard Y. Very-high-speed permanent magnet motors: mechanical rotor stresses analytical model. 2017 IEEE International Electric Machines Drives Conference IEMDC 2017, Miami, FL.

[10] Zhang F, Du G, Wang T, et al. Rotor retaining sleeve design for a 1.12-MW high-speed PM machine. IEEE Trans Ind Appl. 2015;51(5):3675–3685. doi:10.1109/TIA.2015.2423659.

[11] Bredthauer NSJ. Starting of large and medium voltage motors design, protection and safety aspects. IEEE Trans Ind Appl. 1995;131(5):1167–1176.

[12] Finley WR. Troubleshooting induction motors. IEEE Trans Ind Appl. 2000;5:3491–3498.

[13] Alger PL. The nature of polyphase induction machines. New York: Wiley; 1951.

[14] Lecointe PSJ-P, Duchesne S, Romary R, et al. (2006). Insulation aging in AC motors due to mechanical stresses. ICEM 2006, Crete Island, Greece.

[15] Lotzkat W, Stadtfeld S. Controlled AC drives with ride-through capability at power interruption. IEEE Trans Ind Appl. 1994;30(5):1275–1283. doi:10.1109/28.315239.

[16] Lee S-B, Shin J, Park Y, et al. Reliable flux based detection of induction motor rotor faults from the 5th rotor rotational frequency sideband. IEEE Trans Ind Electron; doi:10.1109/TIE.2020.3016241.

[17] Jiang W, Huang W, Lin X, et al. Analysis of rotor Poles and armature winding configurations combinations of wound field flux switching machines. IEEE Trans Ind Electron; doi:10.1109/TIE.2020.3009578.

[18] Liu Y, et al. 3D thermal stress analysis of the rotor of an induction motor. IEEE Trans Magn. July 2000;36(4):1394–1397. doi:10.1109/20.877699.

[19] Zhao N, Zhu ZQ, Liu W. Rotor eddy current loss calculation and thermal analysis of permanent magnet motor and generator. IEEE Trans Magn. Oct. 2011;47(10):4199–4202. doi:10.1109/TMAG.2011.2155042.
[20] Yamazaki K, Watanabe Y. Inter bar current analysis of induction motors using 3-D finite-element method considering lamination of rotor core. IEEE Trans Magn. April 2006;42(4):1287–1290. doi:10.1109/TMAG.2006.871423.
[21] Taghavi S, Pillay P. A novel grain-oriented lamination rotor core assembly for a synchronous reluctance traction motor with a reduced torque ripple algorithm. IEEE Trans Ind Appl. Sept.–Oct. 2016;52(5):3729–3738. doi:10.1109/TIA.2016.2558162.
[22] Gmyrek Z, Vaschetto S, Ahmadi Darmani M, et al. Noninvasive measurements and FEM analyses for estimating the rotor bar-lamination contact resistance. IEEE Trans Ind Appl. Jan.–Feb. 2021;57(1):208–217. doi:10.1109/TIA.2020.3028347.
[23] Goktas T, Arkan M. Discerning broken rotor bar failure from low-frequency load torque oscillation in DTC induction motor drives. Trans Inst Meas Control. 2018;40(1):279–286. doi:10.1177/0142331216654964.
[24] Dias CG, Pereira FH. Broken rotor bars detection in induction motors running at very low slip using a Hall effect sensor. IEEE Sens J. 2018;18(11):4602–4613. doi:10.1109/JSEN.2018.2827204.
[25] Gökhan Yetgin A. Effects of induction motor end ring faults on motor performance. Experimental results. Eng Fail Anal. 2019;96:374–383. DOI:10.1016/j.engfailanal.2018.10.019.
[26] Kumar P, Hati AS. Transfer learning-based deep CNN model for multiple faults detection in SCIM. Neural Comput & Applic. 2021;33:15851–15862. doi:10.1007/s00521-021-06205-1.
[27] Yu W, Jiang D, Wang J, et al. Rotor-current-based fault detection for doubly-fed induction generator using new sliding mode observer. Trans Inst Meas Control. 2020; doi:10.1177/0142331220941009.
[28] Khelfi H, Hamdani S. Induction motor rotor fault diagnosis using three-phase current intersection signal. Electr Eng. 2020;102:539–548. doi:10.1007/s00202-019-00894-7.
[29] Kumar P, Hati AS. Convolutional neural network with batch normalisation for fault detection in squirrel cage induction motor. IET Electr Power Appl. 2021;15:39–50. DOI: 10.1049/elp2.12005.
[30] Liang P, Pei Y, Chai F, et al. Calculation of the maximum mechanical stress on the rotor of interior permanent-magnet synchronous motors. IEEE Trans Ind Electron. 2016;33(6):3420–3432.